fractal and fractional

MDPI

Article

Quantitative Fault Diagnosis of Railway Wheel Polygonization Based on Fractional-Order-Enhanced Transform-Domain Multi-Instance Learning and FiLM Modulation

Tao Li [1], Xuyuan Gao [1], Zhoncheng Jiang [2,3], Wei Liu [4], Dengke Li [2,3], Xuancheng Yuan [2,3,*] and Bowen Yao [2,3]

[1] School of Transportation and Electrical Engineering, Hunan University of Technology, Zhuzhou 412007, China; litao@hut.edu.cn (T.L.); m24081100003@stu.hut.edu.cn (X.G.)
[2] National Key Laboratory for Heavy-Duty High-Power Electric Locomotives Zhuzhou, Zhuzhou 412001, China; 010200004447@crrcgc.cc (Z.J.); ldk@mail.ioa.ac.cn (D.L.); 010200003299@crrcgc.cc (B.Y.)
[3] CRRC Zhuzhou Locomotive Co., Ltd., Zhuzhou 412001, China
[4] Zhuzhou Times New Material Technology Co., Ltd., Zhuzhou 412007, China; liuwei33@csrzic.com
* Correspondence: 010200002091@crrcgc.cc

Abstract

Wheel polygonization is a typical out-of-roundness fault in high-speed trains, and multi-order roughness spectra can quantitatively describe its fault condition. Variations in operating speed, wheel diameter, and reprofiling state cause differences in axle-box vibration responses, making the diagnosis of multi-order roughness amplitudes difficult. A fractional-order-enhanced transform-domain multi-instance learning method with FiLM modulation is proposed for quantitative fault diagnosis of wheel polygonization. First, axle-box vibration acceleration, operating speed, and measured roughness data are jointly processed to construct multi-instance samples containing angular-domain time series, order-domain spectra, vibration statistics, and operating-condition information. Second, a model integrating transform-domain multi-instance learning and FiLM modulation is constructed, combining a state-adaptive multi-regression mechanism with order-aware correlation mapping to achieve quantitative diagnosis of roughness amplitudes across orders 1–32. Finally, the Grünwald–Letnikov fractional-order difference is introduced into the loss function to enhance the model's ability to learn inter-order correlations and overall spectral-shape features, thereby reducing diagnostic errors in multi-order roughness amplitudes. Experimental results show that the proposed method achieves an RMSE of 1.157 dB, 60.5% lower than that of CNN-LSTM, the best-performing comparison method, providing a quantitative diagnostic method for high-speed train wheel condition assessment and reprofiling evaluation.

Keywords: wheel polygonization; quantitative fault diagnosis; fractional-order difference; multi-instance learning; film modulation; axle-box vibration

Academic Editor: Frits Agterberg

Received: 30 September 2026
Revised: 29 October 2026
Accepted: 30 October 2026
Published: 5 November 2026

Copyright: © 2026 by the author. Licensee MDPI, Basel, Switzerland. This article is an open access article distributed under the terms and conditions of the Creative Commons Attribution (CC BY) license.

1. Introduction

Wheel polygonal wear is a common circumferential out-of-roundness fault that develops during the long-term operation of railway vehicles. Its periodic geometric deviations generate rotation-related periodic excitations during wheel–rail contact. As operating speed increases, wheel polygonization may intensify wheel–rail dynamic interactions,

axle-box vibrations, and load fluctuations in critical components, thereby affecting vehicle ride stability and the service reliability of the running gear. At present, wheel polygonization is still primarily assessed through periodic inspections and addressed through reprofiling maintenance, making it difficult to continuously capture detailed changes in fault severity during service. Compared with a single fault identification result, a multi-order roughness spectrum can provide a more detailed description of different order components and their corresponding amplitude levels. Therefore, establishing a reliable mapping between axle-box vibration responses and the multi-order wheel roughness spectrum to achieve quantitative fault diagnosis of wheel polygonization is of considerable significance for wheel condition assessment and maintenance decision-making.

The formation and development of wheel polygonization are intrinsically associated with periodic wheel–rail excitation, structural modal coupling, and wear evolution. Previous studies have systematically investigated vehicle-track coupled dynamics and the evolution of wheel out-of-roundness [1–3]. Ma et al. [4] investigated the formation mechanism and distribution characteristics of high-order wheel polygonization in high-speed railways from the perspective of vehicle-track coupling. Cai et al. [5] conducted long-term tracking tests to analyze the relationships among polygonal passing frequencies, system resonances, and line operating conditions. Liu et al. [6] combined full-scale experiments with numerical simulations to investigate wheelset-gearbox vibration responses under the combined effects of polygonal wear and track irregularities. Further studies have extended the understanding of the formation and evolution of wheel polygonization from the perspectives of thermo-mechanical coupling [7], local rail bending modes [8], and excitation caused by local wheelset defects [9]. These studies provide a theoretical basis for interpreting the physical origins of polygon-related responses in axle-box vibrations; however, their primary focus remains on formation mechanisms and dynamic response characteristics.

Based on these dynamic characteristics, extracting information that reflects wheel out-of-roundness from responses measured during train operation has become an important research topic. Axle-box vibration acceleration has been widely used for wheel polygonization detection because of its high sensitivity to periodic wheel–rail excitation [10–12]. To address non-stationary operating conditions and track-induced disturbances, Xu et al. [13] proposed a weighted angular-domain synchronous moving-average method to suppress track-induced disturbances. Xie et al. [14] employed an improved frequency-domain integration method for quantitative detection of wheel polygonization. For quantitative amplitude inversion, Xu et al. [15] combined cepstral analysis, Bayesian calibration, and frequency response functions to improve the accuracy of quantitative roughness diagnosis, whereas Li et al. [16] developed a wheel out-of-roundness inversion method considering rail flexibility and multi-wheel coupling. Wang et al. [17] established a dynamic detection framework for non-stationary processes based on the discrete Fourier transform. Although these methods are supported by relatively clear physical mechanisms, they generally rely on specific preprocessing procedures, transfer relationships, or dominant-order extraction, and their joint use of multi-window information and multi-order fault characteristics under complex field vibration conditions remains limited.

In field measurements, vibration signals are often affected by non-stationarity, noise interference, and multidimensional feature coupling. Under such conditions, predefined signal features alone are insufficient to fully characterize the complex mapping between vibration responses and wheel conditions. Consequently, data-driven methods have gradually been introduced for wheel out-of-roundness identification and quantitative detection [18,19]. Magalhães et al. [20] employed sparse autoencoders to identify wheel out-of-roundness damage, while Jorge et al. [21] further combined wayside monitoring with stacked sparse autoencoders for early identification. Sun et al. [22] integrated angular-

domain synchronous averaging with CNN regression to estimate polygonal orders and amplitude-related indicators. More recent studies have introduced probabilistic learning [23], physics-guided neural networks [24], and structural-information-assisted generalization mechanisms [25] to improve quantitative inversion performance and adaptability under complex operating conditions. Overall, data-driven methods have gradually evolved from fault identification toward quantitative estimation. However, existing studies mainly focus on polygonal order identification, condition classification, or the estimation of specific amplitude indicators, while quantitative diagnosis of multi-order wheel roughness amplitudes still requires further investigation.

To extract fault information from complex vibration signals, fractional-order methods have been increasingly applied to mechanical fault diagnosis in recent years because of their tunable non-integer orders and ability to incorporate historical information [26–28]. Xu et al. [29] introduced fractional-order derivatives into a stochastic resonance model to enhance weak fault features in wind turbine drivetrains. He et al. [30] further employed fractional-order stochastic resonance to improve the extraction of early mechanical fault features in the presence of strong background noise. Xie et al. [31] used Grünwald–Letnikov fractional-order differentiation to enhance non-stationary vibration information for gearbox fault diagnosis. These studies demonstrate that fractional-order operators can provide additional support for extracting and characterizing complex fault information, thereby offering a potential approach for further exploiting variations in multi-order roughness spectra for quantitative diagnosis of wheel polygonization.

Therefore, to address the differences in axle-box vibration responses caused by variations in operating speed, wheel diameter, and reprofiling state, and the resulting difficulty in diagnosing multi-order roughness amplitudes, this study proposes a fractional-order-enhanced transform-domain multi-instance learning method with FiLM modulation for quantitative fault diagnosis of wheel polygonization (FO-TD-MIL-FiLM). The main contributions are as follows:

1. Axle-box vibration acceleration, operating speed, and measured roughness data are jointly processed. Valid vibration windows are obtained by screening vibration segments based on operating speed and its rate of change, followed by angular-domain resampling and fixed-revolution segmentation. Multiple windows from the same wheel operating state are organized as instances to construct multi-instance samples containing angular-domain time series, order-domain spectra, vibration statistics, and operating-condition information, providing a data basis for quantitative fault diagnosis of wheel polygonization.

2. A model integrating transform-domain multi-instance learning and FiLM modulation is constructed. Attention-based multi-instance aggregation is employed to obtain wheel-state features, which are refined using operating-condition information. A state-adaptive multi-regression mechanism and order-aware correlation mapping are introduced to account for differences between pre- and post-reprofiling stages and inter-order correlations, enabling quantitative diagnosis of wheel polygonization roughness amplitudes across orders 1–32.

3. The Grünwald–Letnikov (G–L) fractional-order difference is introduced into the loss function. Fractional-order-enhanced constraints account for both order-wise amplitude errors and cross-order variation features, enhancing the model's ability to learn inter-order correlations and overall spectral-shape features, thereby reducing errors in the quantitative diagnosis of multi-order roughness spectra.

2. Methodology

To establish a mapping between axle-box vibration responses and the multi-order roughness spectrum of wheel polygonization, a quantitative fault diagnosis method based

on fractional-order-enhanced transform-domain multi-instance learning and FiLM modulation is proposed. The wheel operating state is treated as the basic diagnostic unit, and multiple vibration windows acquired from the same wheel under the same operating state are organized into a multi-instance bag. Angular-domain time-series data, order-domain spectral data, and vibration statistical data are used as feature inputs, while operating-state information, including speed, rotational frequency, and wheel diameter, is used as the conditioning input for FiLM modulation. As shown in Figure 1, the overall framework comprises transform-domain feature extraction, attention-based multi-instance aggregation, FiLM-based conditional modulation, state-adaptive multi-regression, order-aware correlation mapping, and a fractional-order-enhanced joint loss. The model ultimately outputs the wheel roughness amplitude spectrum across orders 1–32, thereby achieving quantitative fault diagnosis of wheel polygonization.

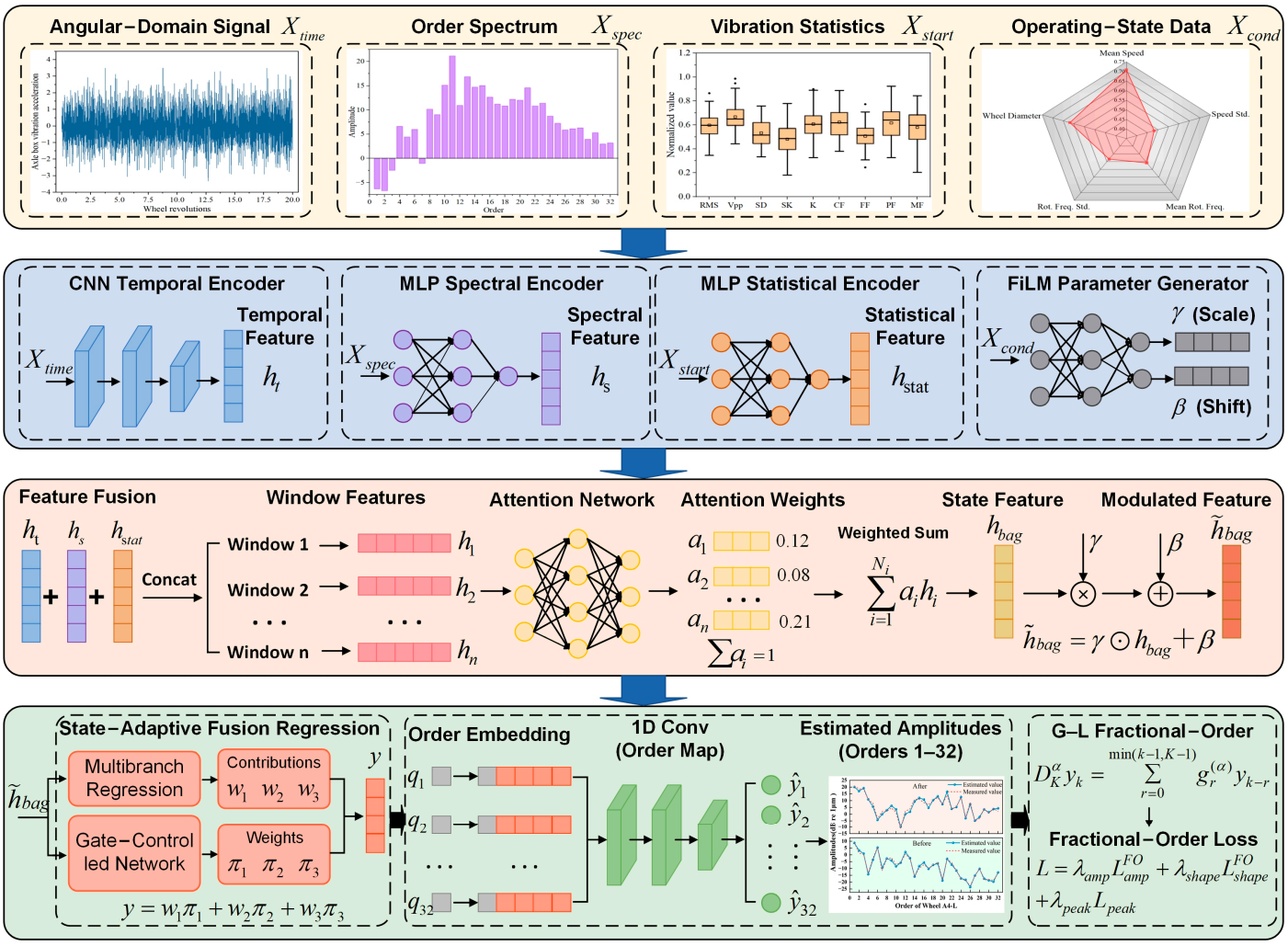


Figure 1. Overall architecture of the FO-TD-MIL-FiLM method.

Let the multi-instance bag corresponding to the s-th wheel state be denoted by B_s, where each instance represents a vibration window containing a fixed number of wheel revolutions, and M_s denotes the number of windows under the corresponding operating state. The multi-instance bag and the diagnostic target can be expressed as [32,33]:

$$B_s = \left\{ \left(x_{s,j}^{t}, x_{s,j}^{o}, x_{s,j}^{r}, c_{s,j} \right) \right\}_{j=1}^{M_s} \tag{1}$$

$$y_s = \left[y_{s1}, y_{s2}, \ldots, y_{s32} \right]^{\mathrm{T}}, \quad \hat{y}_s = F_\theta(B_s) \tag{2}$$

where $x_{s,j}^{t}$, $x_{s,j}^{o}$, $x_{s,j}^{r}$, and $c_{s,j}$ denote the angular-domain time-series data, order-domain spectral data, vibration statistical data, and operating-state data corresponding to the *j*-th window, respectively. y_s denotes the vector of measured roughness amplitudes across orders 1–32, $\hat{y}_s$ represents the diagnostic output of the model for the multi-order roughness amplitudes, and $F_\theta(\cdot)$ denotes the overall diagnostic mapping function. For each instance in the multi-instance bag, a one-dimensional convolutional neural network and two MLPs are employed to extract information from the respective inputs, and the extracted features are then fused to obtain a window-level feature representation:

$$h_{s,j}^{t} = F_t\left(x_{s,j}^{t}\right), h_{s,j}^{o} = F_o\left(x_{s,j}^{o}\right), h_{s,j}^{r} = F_r\left(x_{s,j}^{r}\right) \tag{3}$$

$$h_{s,j} = \sigma\left(W_h\left[h_{s,j}^{t}; h_{s,j}^{o}; h_{s,j}^{r}\right] + b_h\right) \tag{4}$$

A single wheel operating state generally corresponds to multiple vibration windows, whereas an individual window is susceptible to local track excitation, random noise, and speed fluctuations and therefore may not reliably represent the overall wheel condition. To address this issue, an attention-based multi-instance aggregation mechanism is introduced. It assigns weights to different windows according to their contributions to the quantitative diagnosis and aggregates the window-level features into a state-level representation [32]:

$$e_{s,j} = \mathrm{v}_a^{\mathrm{T}} \tanh\left(W_a h_{s,j} + b_a\right), \alpha_{s,j} = \frac{\exp\left(e_{s,j}\right)}{\Sigma_{l=1}^{M_s} \exp\left(e_{s,l}\right)} \tag{5}$$

$$z_s = \sum_{j=1}^{M_s} a_{s,j} h_{s,j} \tag{6}$$

where $\alpha_{s,j}$ denotes the attention weight assigned to the *j*-th window, and z_s represents the wheel state feature. This aggregation process enables the model to obtain a more stable state-level representation from multiple operating segments, thereby reducing its dependence on local information from any single segment. Furthermore, operating-state factors such as speed, rotational frequency, and wheel diameter can alter the amplitude level, frequency positions, and feature distribution of axle-box vibration responses. Therefore, a FiLM modulation mechanism is introduced to adaptively refine the wheel state feature. The operating-state information within the multi-instance bag is first aggregated to obtain the operating-state vector C_s:

$$c_s = \frac{1}{M_s} \sum_{j=1}^{M_s} c_{s,j} \tag{7}$$

The conditional mapping network then generates the scaling parameter γ_s and bias parameter β_s, and feature modulation is performed using a residual FiLM formulation [34,35]:

$$\gamma_s = G_\gamma(c_s), \quad \beta_s = G_\beta(c_s) \tag{8}$$

$$\tilde{z}_s = z_s + \lambda_f(\gamma_s \odot z_s + \beta_s) \tag{9}$$

where $\odot$ denotes element-wise multiplication, λ_f is the modulation intensity coefficient, and $\tilde{z}_s$ denotes the modulated state feature. By incorporating operating-state information into the feature refinement process, the model can adapt the feature representation of axle-box vibration acceleration under different speed levels, rotational frequencies, and wheel diameters, thereby alleviating distribution shifts caused by variations in operating states.

https://doi.org/10.3390/fractalfract10110774

Differences in wheel geometry, wheel diameter, and wheel–rail contact conditions between the pre- and post-reprofiling stages result in different distributions of vibration responses across the two stages. To characterize both the common patterns and stage-specific differences under pre- and post-reprofiling conditions, a state-adaptive multi-regression mechanism is developed. It consists of a shared regression channel, a pre-reprofiling regression channel, and a post-reprofiling regression channel, which jointly generate the multi-order roughness spectrum. A gating network is employed to adaptively generate the fusion weights of the regression channels according to the state feature, operating-state embedding, stage information, and wheel information. The fusion context vector is defined as r_s, and the individual regression channels and their adaptive fusion process are expressed as:

$$\hat{y}_s^c = R^c(r_s), \quad \hat{y}_s^b = R^b(r_s), \quad \hat{y}_s^a = R^a(r_s) \tag{10}$$

$$\pi_s = \mathrm{Softmax}\left(G_g(r_s)\right), \quad \pi_s^c + \pi_s^b + \pi_s^a = 1 \tag{11}$$

$$\hat{y}_s = \pi_s^c \hat{y}_s^c + \pi_s^b \hat{y}_s^b + \pi_s^a \hat{y}_s^a \tag{12}$$

where $R^{\mathrm{c}}(\cdot)$, $R^{\mathrm{b}}(\cdot)$, and $R^{\mathrm{a}}(\cdot)$ denote the shared, pre-reprofiling, and post-reprofiling regression channels, respectively, while $\pi_{\mathrm{s}}^{\mathrm{c}}$, $\pi_{\mathrm{s}}^{\mathrm{b}}$, and $\pi_{\mathrm{s}}^{\mathrm{a}}$ are the fusion weights generated by the gating network. While retaining information common to the pre- and post-reprofiling stages, this mechanism adaptively adjusts the contribution of each regression channel according to the data distribution of the corresponding stage, thereby improving the model's adaptability to differences between reprofiling stages.

To avoid simply treating the 32 orders as mutually independent outputs, an order-aware correlation mapping is further introduced into each regression channel. Learnable order embeddings are first employed to explicitly distinguish the tasks associated with different orders, after which one-dimensional convolution is performed along the order dimension to establish information exchange between neighboring orders. For the *m*-th regression channel, the hidden feature of the *k*-th order and its corresponding correlation mapping can be expressed as:

$$u_{s,k}^m = \varphi_m([r_s; q_k]), \quad k = 1,2,\ldots,32, \quad m \in \{c,b,a\} \tag{13}$$

$$\tilde{U}_s^m = U_s^m + \mathrm{Conv}_{\mathrm{ord}}(U_s^m), \quad \hat{y}_{s,k}^m = H_m\left(\tilde{U}_{s,k}^m\right) \tag{14}$$

where q_k denotes the learnable order embedding corresponding to the *k*-th order, and $U_{\mathrm{s}}^{\mathrm{m}} = \left[u_{s,1}^m, \ldots, u_{s,32}^m\right]$ represents the hidden features arranged along the order dimension. Through order embedding and correlation mapping, the model can exploit local inter-order correlations while preserving the distinct characteristics of individual orders, thereby producing a multi-order roughness spectrum with greater continuity across orders.

The model is trained using a fractional-order-enhanced joint loss function. To further exploit the variation information contained in the multi-order roughness spectrum beyond order-wise amplitude errors, the Grünwald–Letnikov (G–L) fractional-order difference is incorporated into both the amplitude and spectral-shape loss terms. For the roughness spectrum sequence $y = \left[y_1, \ldots, y_{32}\right]$ arranged along the order dimension, the finite-memory G–L fractional-order difference is defined as follows [31,36]:

$$D_K^\alpha y_k = \sum_{r=0}^{\min(k-1, K-1)} g_r^{(\alpha)} y_{k-r} \tag{15}$$

$$g_0^{(\alpha)} = 1, \quad g_r^{(\alpha)} = -\frac{\alpha - r + 1}{r} g_{r-1}^{(\alpha)}, \quad r = 1, \ldots, K-1 \tag{16}$$

where α denotes the fractional order, K is the finite memory length, and $g_r^{(\alpha)}$ represents the fractional-order difference coefficient. Unlike the first-order difference, which only compares adjacent orders, the G–L fractional-order difference associates the current order with multiple preceding orders through decaying weights, allowing the constraint at the k-th order to incorporate variation information from multiple orders. The standard backpropagation procedure of the network is not modified; instead, the fractional-order difference is applied separately to the diagnosed and measured spectra within the loss function.

On this basis, the original joint constraints on the order-wise amplitudes, overall spectral shape, and dominant-peak structure are retained, while the amplitude variations and spectral-shape variations obtained by applying the fractional-order difference are incorporated into the corresponding loss terms. The overall loss function is expressed as:

$$L = \lambda_{amp} L_{amp}^{FO} + \lambda_{shape} L_{shape}^{FO} + \lambda_{peak} L_{peak} \tag{17}$$

$$L_{amp}^{FO} = (1-\rho) L_{amp}(y, \hat{y}) + \rho L_{amp}(D^{\alpha} y, D^{\alpha} \hat{y}) \tag{18}$$

$$L_{shape}^{FO} = (1-\rho) L_{shape}(y, \hat{y}) + \rho L_{shape}(D^{\alpha} y, D^{\alpha} \hat{y}), \quad L_{peak} = D_{\mathrm{KL}}\left(p_y \,\|\, p_{\hat{y}}\right) \tag{19}$$

where L_{amp} denotes the order-wise weighted SmoothL1 amplitude loss, L_{shape} is the spectral-shape consistency loss based on cosine similarity, and L_{peak} represents the dominant-peak constraint based on the soft peak distribution and Kullback–Leibler divergence. The parameter ϱ denotes the fractional-order mixing ratio, while λ_{amp}, λ_{shape}, and λ_{peak} are the weights assigned to the corresponding loss terms. In this manner, the model is simultaneously constrained in both the original amplitude space and the fractional-order variation domain, enabling the training process to account for order-wise amplitude accuracy, multi-order variation characteristics, and overall spectral-shape consistency.

Overall, the proposed method takes the multi-instance bag corresponding to each wheel operating state as the basic diagnostic unit. State-level features are obtained through transform-domain encoding of multi-source information and attention-based multi-instance aggregation, while FiLM modulation is employed to alleviate differences in vibration responses caused by variations in operating states. The state-adaptive multi-regression mechanism and order-aware correlation mapping are then combined to obtain the roughness amplitude spectrum across orders 1–32. Finally, the fractional-order-enhanced joint loss further constrains multi-order variation information, resulting in an end-to-end model for quantitative fault diagnosis of wheel polygonization.

3. Dataset Construction

Wheel polygonal wear is characterized by periodic or localized geometric deviations of the wheel circumferential profile from an ideal circular profile. Such out-of-roundness generates periodic excitation associated with wheel rotation during wheel–rail contact and consequently causes variations in axle-box vibration acceleration. To ensure that the data used for subsequent model training can reflect the actual wheel condition, the spatial distributions of wheel out-of-roundness in the pre- and post-reprofiling stages are first analyzed. As shown in Figure 2, the pre-reprofiling wheel profile exhibits pronounced nonuniform deviations over the entire circumference, with relatively large local deviations from the ideal circular profile. In the post-reprofiling stage, the overall wheel profile

becomes smoother, although certain residual fluctuations remain. This indicates that a reprofiled wheel should not simply be regarded as an ideal circular wheel, but rather as a wheel in a distinct post-reprofiling stage.

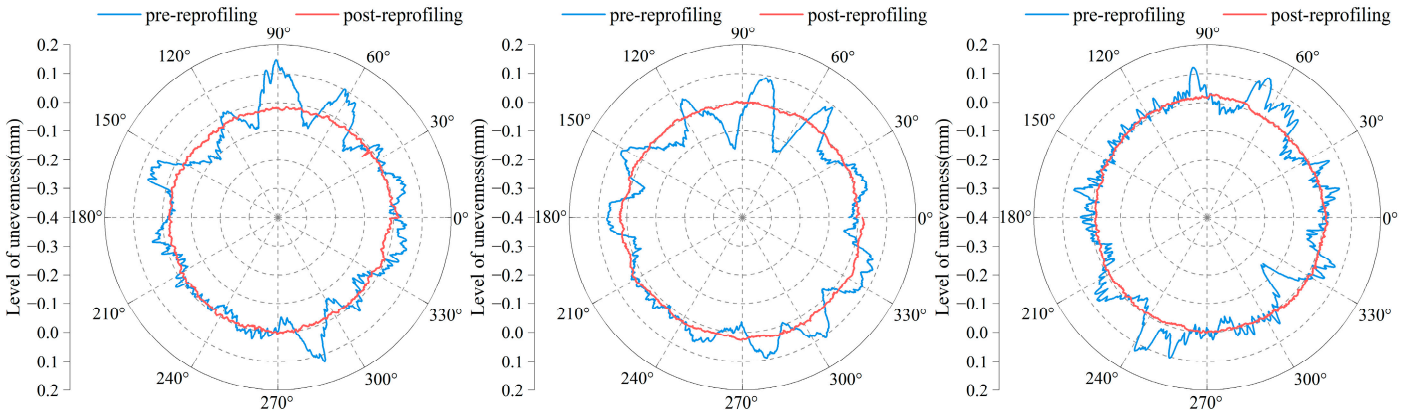


Figure 2. Comparison of wheel out-of-roundness amplitudes in the pre- and post-reprofiling stages.

Based on the above characteristics, a dataset for quantitative fault diagnosis of wheel polygonization is constructed according to the procedure shown in Figure 3. The study includes 12 wheels from two types of high-speed trains. The data for each wheel cover two stages, namely pre-reprofiling and post-reprofiling, with six operating states in each stage. The axle-box vibration acceleration is sampled at 2048 Hz, while the train operating speed is sampled at 4 Hz. Meanwhile, the circumferential out-of-roundness profile under each operating state is measured using a wheel out-of-roundness measurement system. Order analysis is subsequently performed to obtain the roughness amplitude spectrum across orders 1–32, which serves as the reference for quantitative diagnosis of the corresponding wheel state. The roughness amplitudes are expressed in decibels relative to 1 μm (dB re 1 μm), and the model uses the roughness amplitudes across orders 1–32 on this logarithmic scale as its quantitative diagnostic targets.

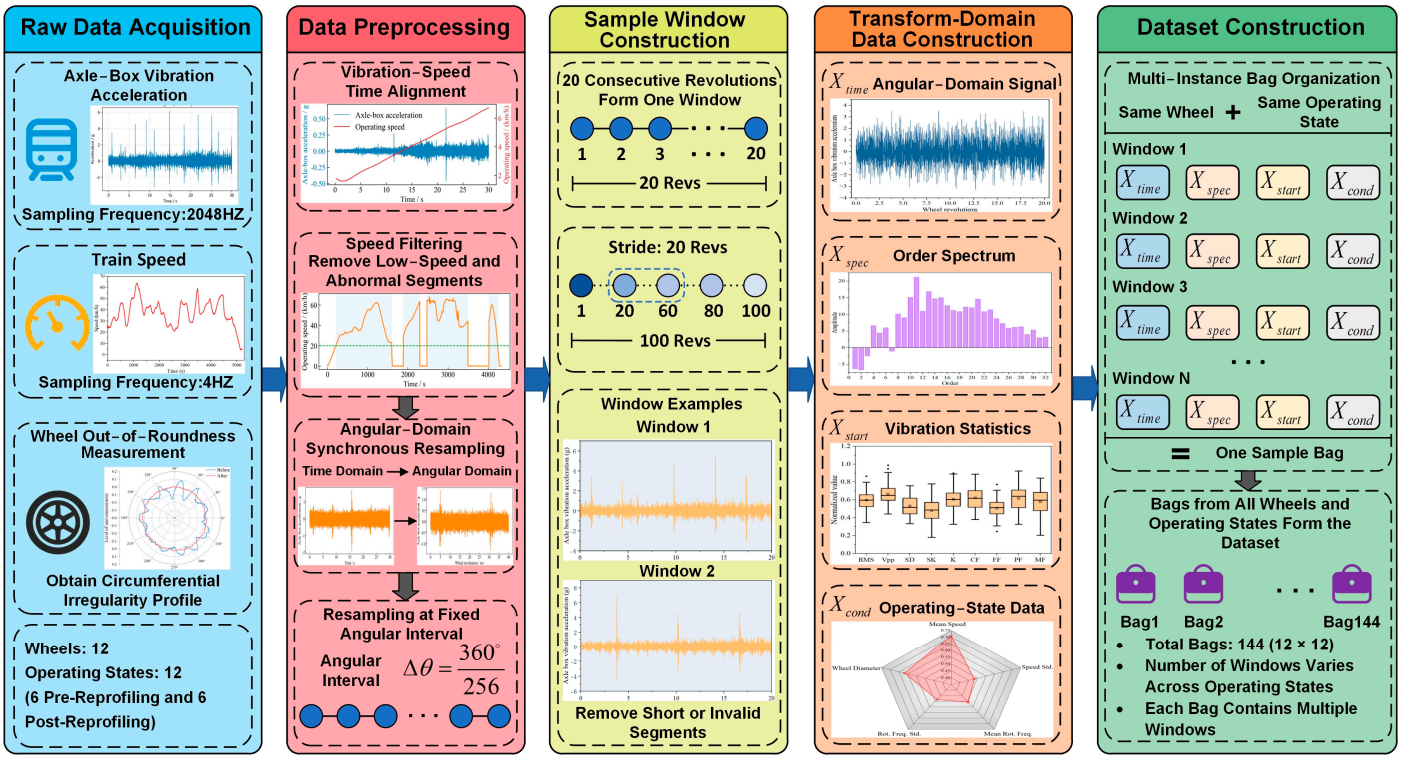


Figure 3. Construction procedure of the dataset for wheel polygonization quantitative fault diagnosis.

During data preprocessing, multiple vibration segments corresponding to the same wheel state are first loaded, temporally aligned, and concatenated, while the speed sequence is smoothed. Because the sampling frequency of the speed data is lower than that of the vibration data, the speed information is interpolated onto the vibration signal time axis so that each vibration sample is associated with a corresponding operating speed. Valid data segments are then selected according to the operating speed and its rate of change. Only intervals with an operating speed of no less than 20 km/h, an absolute rate of speed change of no more than 2.0 km/h/s, and a continuous duration longer than 8 s are retained. This procedure reduces the effects of low-speed operation, rapid speed variations, and abnormal speed fluctuations on the stability of the extracted vibration characteristics.

To improve the consistency of samples acquired under different speed conditions, the instantaneous angular velocity is calculated from the operating speed and wheel diameter, and the wheel angular displacement is then obtained by integration. The axle-box vibration signal is thereby transformed from the time domain into the angular domain. Angular-domain resampling enables the vibration response to be uniformly described with respect to the wheel rotation angle, thereby improving the comparability of samples obtained at different operating speeds. In this study, each wheel revolution is resampled at 256 equally spaced angular points. Twenty consecutive revolutions are used to form one sample window, and the window stride is also set to 20 revolutions, resulting in an angular-domain vibration sequence with a length of 5120 samples. On this basis, angular-domain time-series data, order-domain spectral data, vibration statistical data, and operating-state information are further organized for each vibration window. The vibration statistical data include the root-mean-square (RMS) value, peak-to-peak value, standard deviation, skewness, kurtosis, crest factor, waveform factor, impulse factor, and clearance factor. The operating-state information includes mean speed, speed standard deviation, mean rotational frequency, rotational-frequency standard deviation, and wheel diameter.

The processed vibration windows are organized using a multi-instance learning framework. For the same wheel, reprofiling stage, and operating state, multiple fixed-revolution vibration windows are grouped into a multi-instance bag, with each vibration window serving as an individual instance. The entire bag corresponds to the roughness amplitude spectrum across orders 1–32 of the corresponding wheel state. This organization preserves the differences among vibration windows acquired under the same operating state and avoids relying on a single window to represent the overall wheel condition.

Accordingly, a multi-instance dataset integrating angular-domain time-series data, order-domain spectral data, vibration statistical information, and operating-state information is ultimately constructed. Among these inputs, the angular-domain time-series data, order-domain spectral data, and vibration statistical information serve as the primary feature inputs to FO-TD-MIL-FiLM, whereas the operating-state information is used for subsequent FiLM-based conditional modulation. The corresponding measured roughness amplitude spectrum across orders 1–32 is used as the quantitative diagnostic reference, providing a basis for subsequent model training and performance evaluation.

The above axle-box vibration acceleration, train operating speed, and wheel circumferential out-of-roundness profiles were obtained from field measurements of high-speed trains, covering different operating states and wheel out-of-roundness characteristics in the pre- and post-reprofiling stages. After constructing the multi-instance samples, the training, validation, and test sets were separately divided for each wheel according to different operating states at a ratio of 4:1:1, and were used for model training,

hyperparameter tuning, and final diagnostic performance evaluation, respectively. All vibration windows corresponding to the same operating state were assigned to only one data subset to prevent information leakage caused by similar windows appearing across different subsets. The training, validation, and test sets contained the same physical wheels but corresponded to mutually independent operating states, allowing the quantitative fault diagnosis capability of the model to be evaluated for previously seen wheels under different operating states and both pre- and post-reprofiling conditions.

4. Experimental Analysis

To evaluate the effectiveness of FO-TD-MIL-FiLM for quantitative fault diagnosis of wheel polygonization, model training and performance evaluation are conducted based on the dataset partition described above. The measured 1st–32nd-order wheel roughness amplitude spectra are used as the quantitative diagnostic reference. Model performance is evaluated mainly in terms of multi-order roughness spectrum fitting, residual distribution, diagnostic errors across different orders, diagnostic errors across different wheels, and comparisons with other methods. In the experiments, FO-TD-MIL-FiLM is compared with CNN-LSTM, Transformer, GRU, OORNet, and ADSA-CNN. All error metrics are calculated directly from the diagnosed and measured roughness amplitudes on the dB scale, without conversion to the linear amplitude domain (μm).

4.1. Quantitative Diagnosis of Multi-Order Roughness Spectra

Figure 4 compares the diagnosed and measured values for different wheels in the test set in the pre- and post-reprofiling stages. FO-TD-MIL-FiLM closely follows the overall trend of the measured multi-order roughness spectra and shows good agreement across most wheels and orders. In the pre-reprofiling stage, the wheel roughness amplitudes are generally higher, with pronounced local peaks at certain orders. The diagnosed roughness spectra can accurately capture the positions of the major peaks and valleys as well as their amplitude variations. In the post-reprofiling stage, although the overall roughness amplitudes decrease, fluctuations remain at certain orders, and the model still demonstrates good tracking performance.

Across different wheels, the diagnostic curves are generally consistent with the measured curves in terms of both the overall variation trend and the positions of the major spectral peaks. This indicates that FO-TD-MIL-FiLM can extract effective information related to the multi-order roughness characteristics of wheel polygonization from multi-instance axle-box vibration data. Certain deviations remain at some higher orders or at orders with abrupt local variations, which may be associated with the complex variation in high-order roughness, fluctuations in operating states, and vibration noise. Overall, however, the model can effectively capture the characteristics of roughness spectra across orders 1–32, demonstrating its capability for quantitative fault diagnosis of wheel polygonization.

4.2. Fractional-Order Difference Ablation Study

To evaluate the effectiveness of the G–L fractional-order difference in quantitative fault diagnosis of wheel polygonization, four ablation experiments are conducted, including the baseline model, first-order difference, second-order difference, and G–L fractional-order difference. The baseline model does not introduce difference constraints, while the other three groups employ different difference constraints. The diagnostic performance of these methods is compared under the same model architecture and experimental settings, as shown in Figure 5.

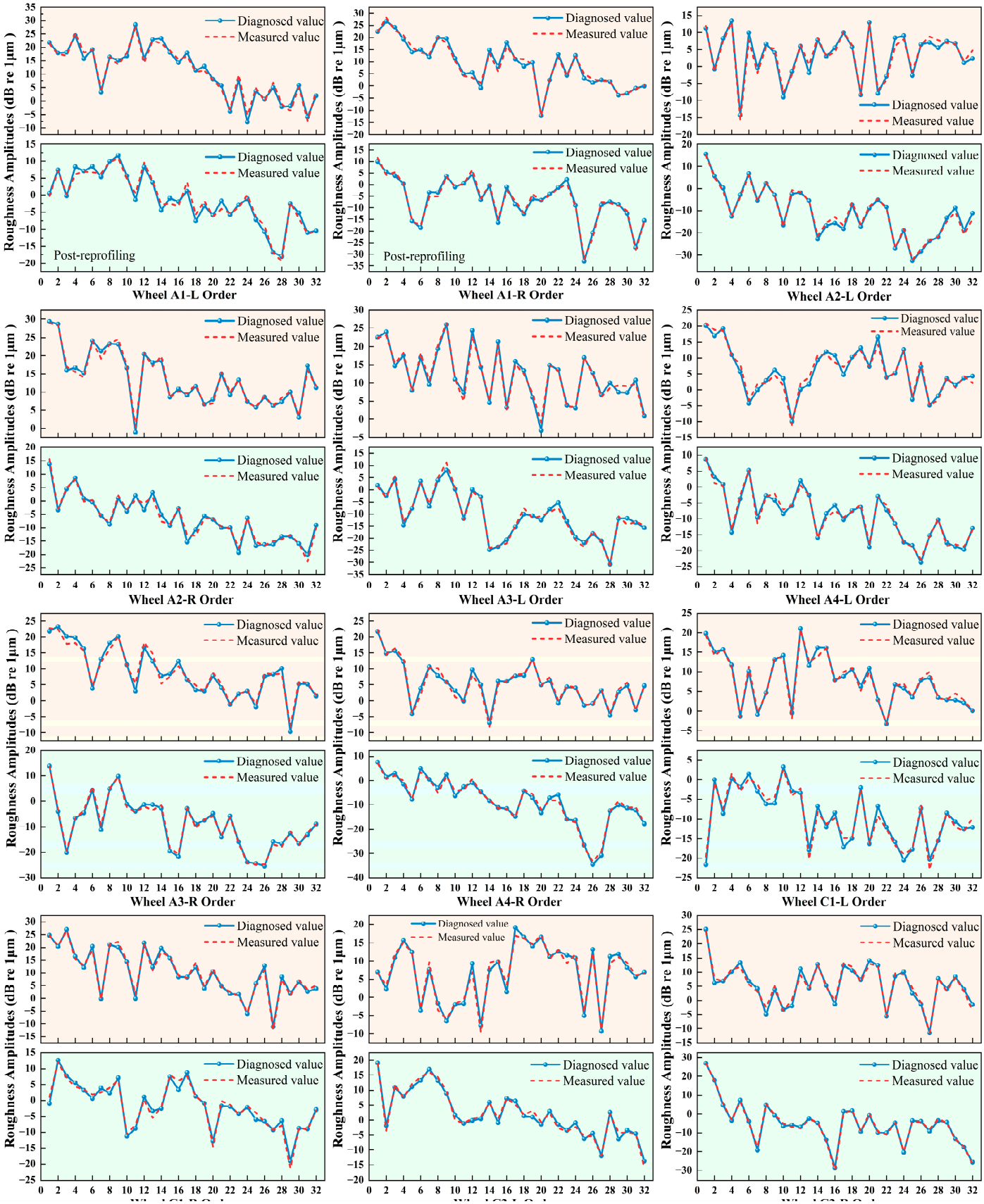


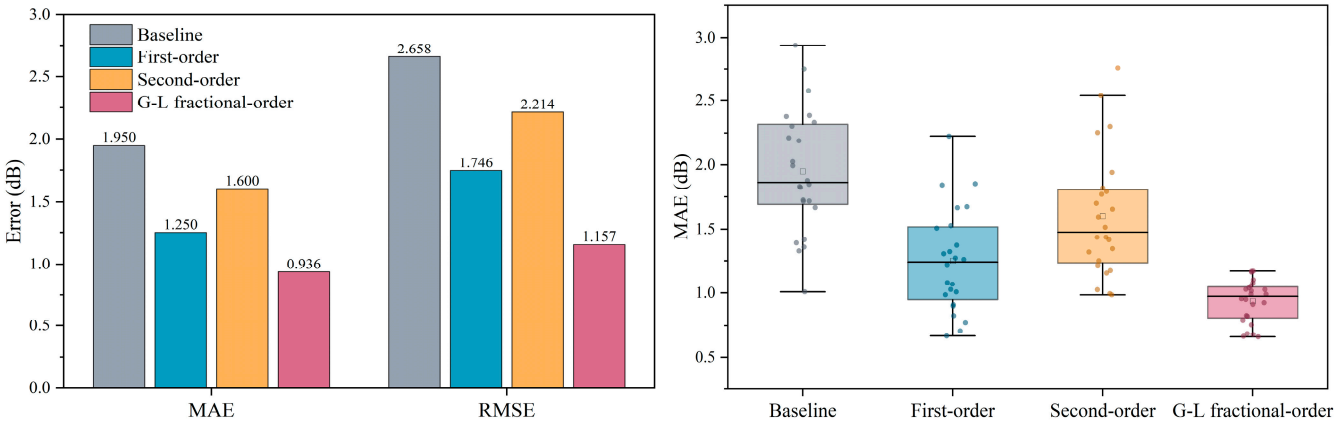
Figure 4. Comparison of diagnosed and measured multi-order roughness spectra for different wheels in the pre- and post-reprofiling stages. The orange and green backgrounds indicate the pre-reprofiling and post-reprofiling stages, respectively.

Figure 5a compares the overall errors of different difference methods. The baseline model achieves an MAE of 1.950 dB and an RMSE of 2.658 dB. After introducing the first-order difference, the MAE and RMSE decrease to 1.250 dB and 1.746 dB, respectively, while the corresponding values for the second-order difference are 1.600 dB and 2.214 dB. In comparison, the G–L fractional-order difference achieves the lowest diagnostic errors, with an MAE of 0.936 dB and an RMSE of 1.157 dB, representing reductions of 52.0% and 56.5%, respectively, compared with the baseline model.

Figure 5b further compares the MAE distributions of different methods. The baseline model exhibits a relatively dispersed error distribution. Both the first-order and second-order differences improve the error distribution to some extent, but certain error fluctuations remain. The G–L fractional-order difference achieves lower overall MAE values with a more concentrated boxplot distribution, indicating that it can effectively reduce diagnostic errors and improve the stability of the results.

Figure 5c presents the diagnostic results of different difference methods for roughness spectra across orders 1–32. The baseline model exhibits noticeable amplitude deviations at certain orders. Although the first-order and second-order differences improve the fitting of local spectral shapes, overestimation or underestimation still occurs at some peak and valley positions. In comparison, the diagnostic curve obtained using the G–L fractional-order difference is closer to the measured spectrum and better captures the main peak and valley positions and their amplitude characteristics.

Figure 5d further illustrates the MAE variations in different methods across orders 1–32. The baseline model exhibits relatively large errors at certain orders, while the errors of the first-order and second-order differences still fluctuate across different orders. In contrast, the G–L fractional-order difference maintains lower MAE values at most orders, with relatively stable error variations. Overall, the G–L fractional-order difference can account for both order-wise amplitude errors and inter-order correlations, enhancing the model's ability to learn multi-order roughness spectra and thereby reducing errors in quantitative fault diagnosis of wheel polygonization.



(**a**) (**b**)

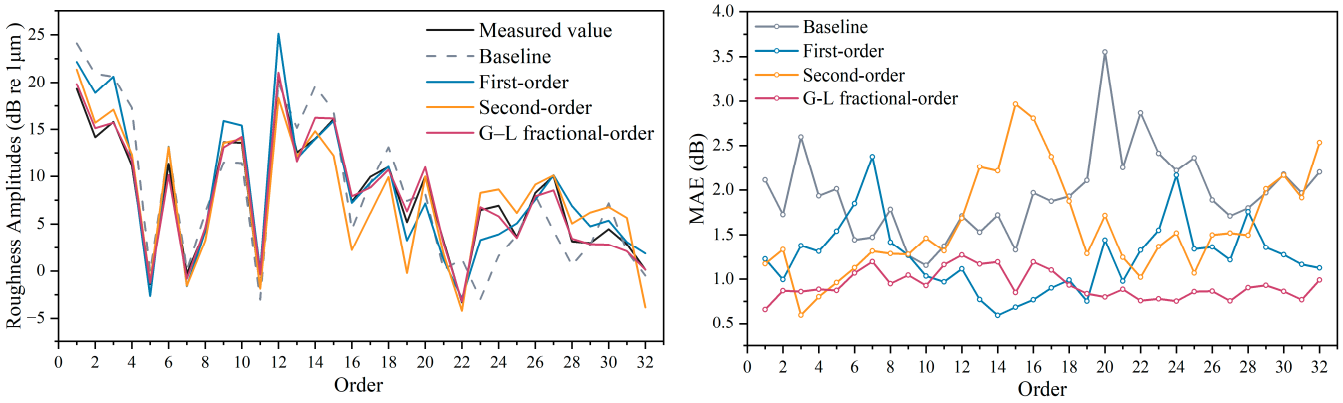


Figure 5. Comparison of fractional-order difference ablation results: (**a**) comparison of MAE and RMSE for different difference methods; (**b**) MAE distributions of different difference methods; (**c**) comparison of diagnosed and measured multi-order roughness amplitude spectra; and (**d**) MAE comparison across orders 1–32 for different difference methods.

4.3. Multidimensional Error and Method Comparison Analysis

Figure 6 presents the diagnostic errors of FO-TD-MIL-FiLM and its comparison with other methods from multiple perspectives. Figure 6a shows the scatter distribution of diagnostic residuals against measured roughness amplitudes. The residuals are mainly concentrated within ±3 dB and distributed around zero, without an obvious systematic bias.

Figure 6b illustrates the MAE distribution across orders 1–32, with the mean MAE of individual orders ranging approximately from 0.7 to 1.3 dB. The error at the 12th order is relatively high, at approximately 1.25 dB, while the remaining orders generally maintain lower error levels. No consistent increase in error is observed with increasing order, indicating that the model maintains relatively stable quantitative diagnostic performance across different orders.

Figure 6c further compares the MAE of different methods across 12 wheels. FO-TD-MIL-FiLM achieves lower diagnostic errors than the other comparison methods for all wheels, with an overall MAE of 0.936 dB. In contrast, the MAE of CNN-LSTM ranges from 1.509 to 3.375 dB, while the other methods exhibit larger diagnostic deviations for certain wheels. For example, for wheel C2-L, FO-TD-MIL-FiLM achieves an MAE of only 0.970 dB, whereas CNN-LSTM and ADSA-CNN reach 3.375 and 8.794 dB, respectively. These results indicate that the proposed method can effectively accommodate differences among wheels and operating states while maintaining low diagnostic errors.

Figure 6d compares the diagnostic error distributions of different methods using the empirical cumulative distribution function (ECDF) of absolute errors based on five repeated experiments, where the curves and shaded bands represent the mean and standard deviation, respectively. FO-TD-MIL-FiLM exhibits the steepest cumulative distribution curve, with a 95th-percentile absolute error (P95AE) of 2.23, indicating that 95% of diagnostic points have absolute errors no greater than 2.23 dB. In comparison, the P95AE values of CNN-LSTM, Transformer, OORNet, GRU, and ADSA-CNN are 5.90, 8.05, 9.88, 10.76, and 11.44 dB, respectively. Compared with CNN-LSTM, the best-performing comparison method, the proposed method reduces P95AE by 62.2%, indicating that more diagnostic errors are maintained within a smaller range, thereby effectively reducing large-amplitude deviations.

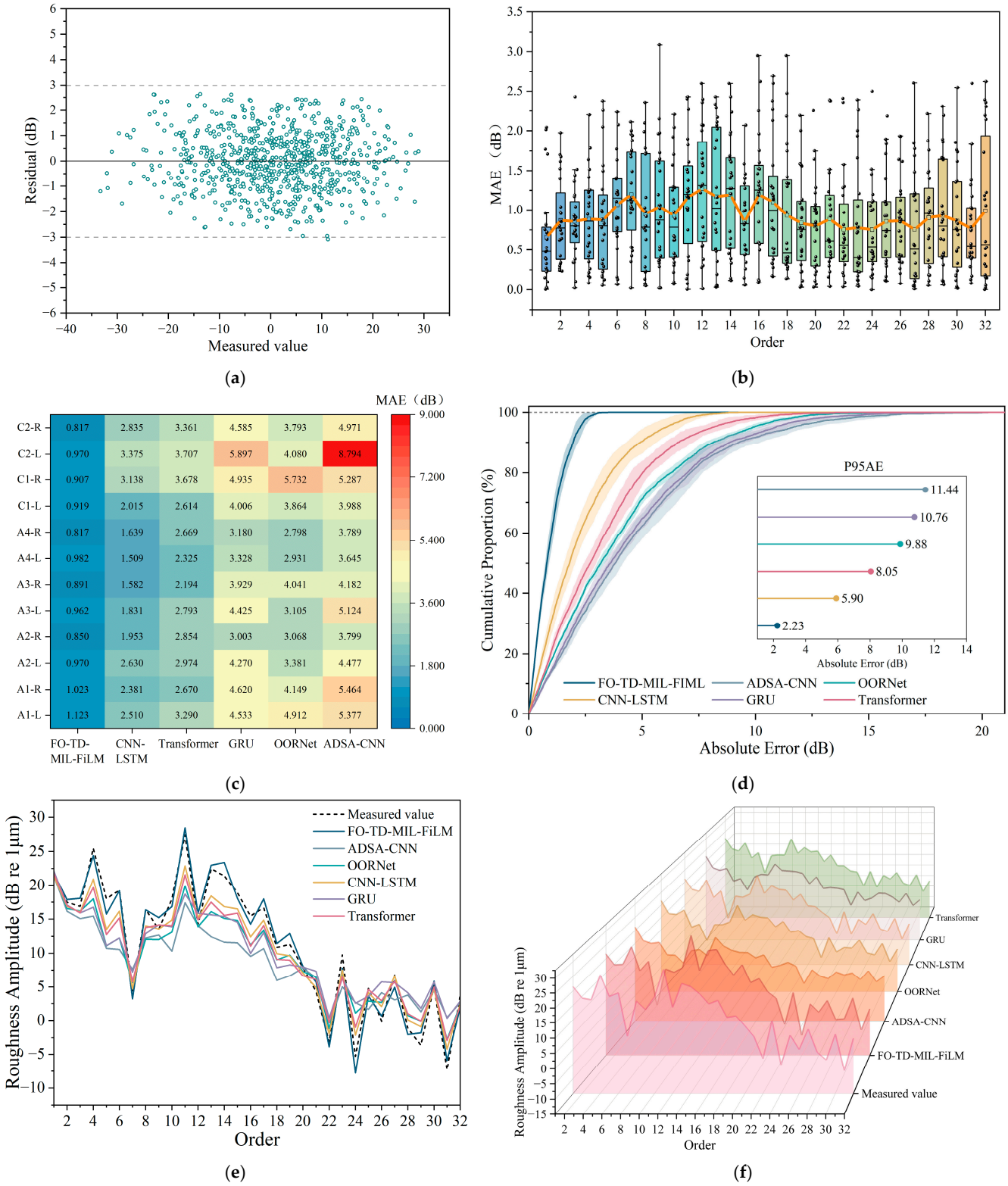


Figure 6. Multidimensional error analysis and method comparison for quantitative fault diagnosis of wheel polygonization: (**a**) scatter distribution of diagnostic residuals versus measured roughness amplitudes; (**b**) MAE boxplots across orders 1–32 , with the orange line indicating the mean values; (**c**) MAE comparison across 12 wheels for different methods; (**d**) empirical cumulative distribution functions of absolute diagnostic errors for different methods over five repeated experiments, with mean curves and standard deviation bands; (**e**) two-dimensional comparison of diagnosed and measured roughness amplitude spectra for different methods; and (**f**) three-dimensional comparison of diagnosed and measured roughness amplitude spectra for different methods.

https://doi.org/10.3390/fractalfract10110774

Figure 6e,f compare the diagnostic results of different methods using two-dimensional roughness spectrum curves and three-dimensional spectral distributions, respectively. As shown in Figure 6e, the diagnostic curve of FO-TD-MIL-FiLM closely matches the measured spectrum, effectively capturing the main peak and valley positions and amplitude variations. Taking the dominant peak at the 11th order as an example, the measured amplitude is approximately 28 dB re 1 μm, and the diagnostic result of the proposed method is close to this value, whereas the diagnosed amplitudes of the other methods are mostly between 18 and 23 dB re 1 μm, showing varying degrees of underestimation. Figure 6f further illustrates the differences in overall spectral shapes among the methods across orders 1–32, with FO-TD-MIL-FiLM showing better tracking of the main spectral peaks and local amplitude variations. Considering the results across different orders, wheels, and cumulative error distributions, the proposed method effectively reduces diagnostic errors in multi-order roughness amplitudes and achieves quantitative fault diagnosis of wheel polygonization.

4.4. Scatter Distribution and Error Metrics

Figure 7 shows the scatter distributions of diagnosed versus measured values for different methods, together with the evaluation metrics MAE, MSE, RMSE, and MAXAE. Scatter points closer to the ideal diagonal line indicate greater consistency between the diagnosed and measured results. The scatter points obtained by FO-TD-MIL-FiLM are generally more concentrated around the ideal diagonal line and exhibit less dispersion across different amplitude ranges, indicating that the proposed method can reliably diagnose the multi-order roughness amplitudes of wheel polygonization. In comparison, the scatter distributions of ADSA-CNN, OORNet, and GRU are relatively dispersed, with noticeable deviations in some amplitude ranges. Although the results of CNN-LSTM and Transformer are comparatively concentrated, their overall dispersion remains greater than that of FO-TD-MIL-FiLM. The green and red histograms, together with their fitted normal curves, illustrate the distributions of measured and diagnosed values, respectively. FO-TD-MIL-FiLM exhibits good consistency between these distributions, further demonstrating its diagnostic accuracy.

In terms of the overall error metrics, FO-TD-MIL-FiLM achieves an MAE of 0.936 dB, an MSE of 1.339 dB^2, an RMSE of 1.157 dB, and a MAXAE of 3.086 dB. In particular, its RMSE is 60.5% lower than that of CNN-LSTM, the best-performing comparison method. The relatively low MAE and RMSE indicate good overall diagnostic accuracy, while the low MSE suggests that large diagnostic errors are effectively controlled. The relatively low MAXAE further indicates that extreme diagnostic deviations are limited. For practical wheel condition assessment, these error levels indicate that the model can effectively capture the overall distribution and major peak characteristics of the roughness amplitude spectrum across orders 1–32, providing a quantitative reference for comparing wheel out-of-roundness in the pre- and post-reprofiling stages, identifying dominant orders, and evaluating reprofiling effectiveness. Considering the results across different amplitude ranges, wheels, and orders, FO-TD-MIL-FiLM can reliably diagnose wheel roughness amplitudes across orders 1–32, demonstrating its capability for quantitative fault diagnosis of wheel polygonization.

https://doi.org/10.3390/fractalfract10110774

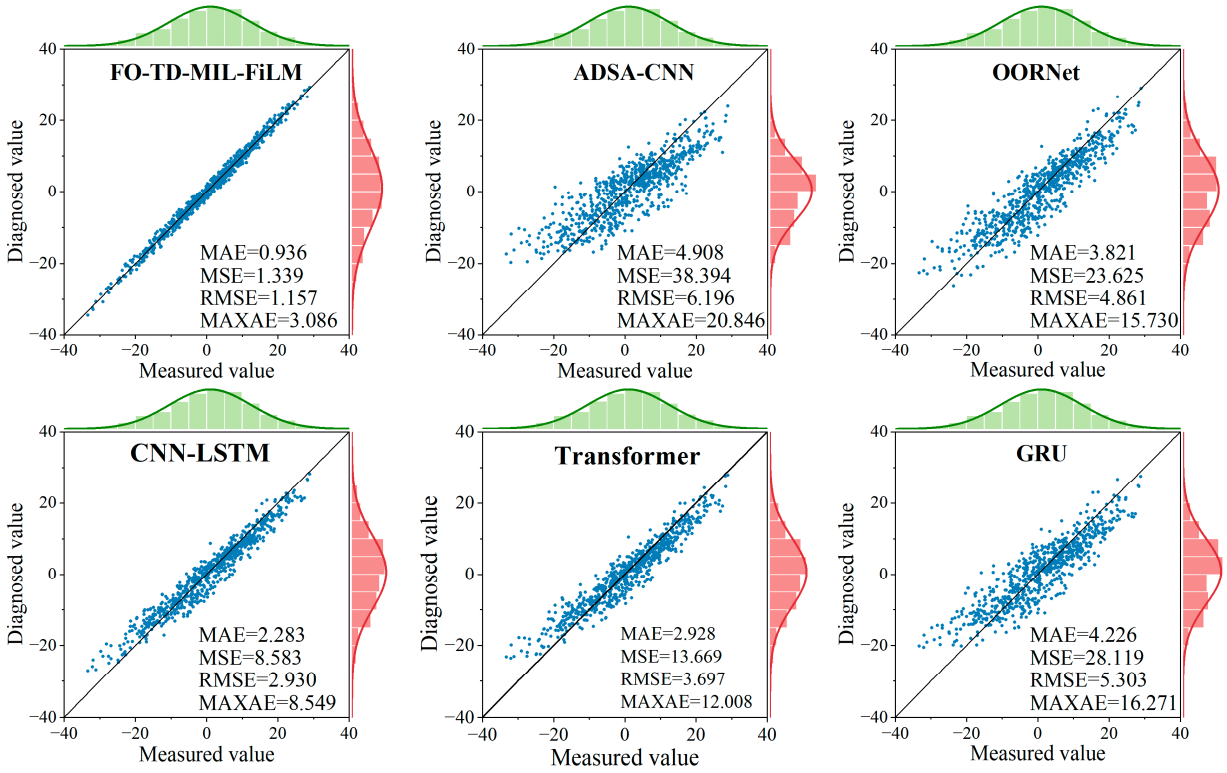


Figure 7. Scatter distributions of diagnosed versus measured values and overall error metrics for different methods, with green and red histograms and fitted normal curves representing the distributions of measured and diagnosed values, respectively.

5. Discussion

Variations in high-speed train operating speed, wheel diameter, and reprofiling stage can affect the mapping relationship between axle-box vibration responses and wheel polygonization roughness amplitudes. FO-TD-MIL-FiLM aggregates information from multiple vibration windows under the same operating state and incorporates FiLM-based conditional modulation, a state-adaptive multi-regression mechanism, and order-aware correlation mapping to account for differences in operating conditions and correlations among different orders. Comparative experiments demonstrate that the proposed method achieves superior performance in terms of overall diagnostic errors and diagnostic results across different wheels, indicating that multi-window information fusion and operating-state-adaptive feature adjustment contribute to improving the quantitative diagnosis of multi-order roughness amplitudes.

The fractional-order difference ablation study demonstrates that the G–L fractional-order difference achieves lower MAE and RMSE values than the configurations without difference constraints or with first- and second-order differences. Compared with integer-order differences, the G–L fractional-order difference establishes relationships between the current order and multiple preceding orders through weighting coefficients. Incorporating it into the amplitude loss and spectral-shape loss of the joint loss function provides more flexible constraints for learning inter-order correlations and overall spectral-shape characteristics, thereby improving the diagnostic performance for multi-order roughness amplitudes.

During actual high-speed train operation, factors such as track irregularities, load variations, and wheel–rail contact conditions may still affect axle-box vibration characteristics. This study investigates 12 physical wheels from two types of high-speed trains. Although the training and test sets contain the same physical wheels, they correspond to different operating states. Therefore, the generalization capability of the model to

previously unseen wheels and a broader range of operating conditions requires further validation. In addition, the computational cost of multi-window feature encoding increases with the number of instances, whereas the fractional-order difference primarily increases the computational demand during training. Future work will focus on expanding the measured dataset and optimizing the model architecture to further improve its generalization capability and applicability in engineering practice.

6. Conclusions

To address the challenges of diagnosing multi-order roughness amplitudes arising from variations in axle-box vibration responses under different operating states and reprofiling stages, this study proposes a quantitative fault diagnosis method for wheel polygonization based on fractional-order-enhanced transform-domain multi-instance learning and FiLM modulation (FO-TD-MIL-FiLM). The proposed method is experimentally validated using field data collected from high-speed trains. The main conclusions are as follows:

(1) The proposed method enables quantitative diagnosis of wheel polygonization roughness amplitudes across orders 1–32, achieving an MAE of 0.936 dB and an RMSE of 1.157 dB on the test set. Compared with CNN-LSTM, Transformer, GRU, OORNet, and ADSA-CNN, the proposed method achieves superior overall diagnostic performance. In particular, its RMSE is 60.5% lower than that of CNN-LSTM, the best-performing comparison method, indicating that the proposed method can effectively improve the diagnostic accuracy of multi-order roughness amplitudes under different operating states.

(2) The G–L fractional-order difference effectively improves the diagnostic performance for multi-order roughness amplitudes. Ablation experiments demonstrate that, compared with the baseline configuration without difference constraints, the introduction of the G–L fractional-order difference reduces the MAE from 1.950 dB to 0.936 dB and the RMSE from 2.658 dB to 1.157 dB, corresponding to reductions of 52.0% and 56.5%, respectively. The G–L fractional-order difference also achieves better overall performance than the first- and second-order difference configurations, confirming the effectiveness of fractional-order difference constraints in the quantitative diagnosis of multi-order roughness amplitudes.

(3) Experimental validation using field data from high-speed trains demonstrates that the proposed method provides a useful reference for quantitatively assessing wheel out-of-roundness caused by polygonization and shows potential for engineering applications. However, due to the limited number of wheel samples and operating conditions, the generalization capability of the model to previously unseen wheels and a broader range of operating conditions requires further validation. Future work will focus on expanding the measured dataset and optimizing the computational cost of the model to further improve its applicability and engineering application potential.

Author Contributions: Conceptualization, T.L., X.G. and X.Y.; methodology, T.L. and X.G.; software, X.G.; validation, T.L., X.G., X.Y. and B.Y.; formal analysis, T.L., X.G. and X.Y.; investigation, Z.J., W.L. and D.L.; resources, W.L. and D.L.; writing—original draft preparation, T.L. and X.G.; writing—review and editing, T.L., X.G., Z.J., W.L., D.L., X.Y. and B.Y.; visualization, X.G.; supervision, X.Y.; project administration, Z.J. and B.Y.; funding acquisition, T.L. All authors have read and agreed to the published version of the manuscript.

Funding: This research was funded by the National Natural Science Foundation of China (62373142 and 52572375); the Natural Science Foundation of Hunan Province, China (2024JJ7129); and the State Key Laboratory of Heavy-duty and Express High-power Electric Locomotives (QZKFKT2025-07).

Data Availability Statement: The data presented in this study are available upon request from the corresponding author.

Conflicts of Interest: Authors Zhoncheng Jiang, Dengke Li, Xuancheng Yuan, and Bowen Yao were employed by the company CRRC Zhuzhou Locomotive Co., Ltd. Author Wei Liu was employed by the company Zhuzhou Times New Material Technology Co., Ltd. The authors declare that the research was conducted in the absence of any commercial or financial relationships that could be construed as potential conflicts of interest.

References

1. Tao, G.; Wen, Z.; Jin, X.; Yang, X. Polygonisation of Railway Wheels: A Critical Review. *Rail. Eng. Sci.* **2020**, *28*, 317–345. https://doi.org/10.1007/s40534-020-00222-x.
2. Iwnicki, S.; Nielsen, J.C.O.; Tao, G. Out-of-Round Railway Wheels and Polygonisation. *Veh. Syst. Dyn.* **2023**, *61*, 1787–1830. https://doi.org/10.1080/00423114.2023.2194544.
3. Yang, Y.; Ling, L.; Wang, C.; Liu, Z.; Wang, K.; Zhai, W. Wheel/Rail Dynamic Interaction Induced by Polygonal Wear of Locomotive Wheels. *Veh. Syst. Dyn.* **2022**, *60*, 211–235. https://doi.org/10.1080/00423114.2020.1807572.
4. Ma, C.; Gao, L.; Cui, R.; Xin, T. The Initiation Mechanism and Distribution Rule of Wheel High-Order Polygonal Wear on High-Speed Railway. *Eng. Fail. Anal.* **2021**, *119*, 104937. https://doi.org/10.1016/j.engfailanal.2020.104937.
5. Cai, W.; Chi, M.; Wu, X.; Sun, J.; Zhou, Y.; Wen, Z.; Liang, S. A Long-Term Tracking Test of High-Speed Train with Wheel Polygonal Wear. *Veh. Syst. Dyn.* **2021**, *59*, 1735–1758. https://doi.org/10.1080/00423114.2020.1786592.
6. Liu, P.; Yang, S.; Liu, Y. Full-Scale Test and Numerical Simulation of Wheelset-Gear Box Vibration Excited by Wheel Polygon Wear and Track Irregularity. *Mech. Syst. Signal Proc.* **2022**, *167*, 108515. https://doi.org/10.1016/j.ymssp.2021.108515.
7. He, C.; Yang, Z.; Zhang, P.; Li, S.; Naeimi, M.; Dollevoet, R.; Li, Z. A Finite Element Thermomechanical Analysis of the Development of Wheel Polygonal Wear. *Tribol. Int.* **2024**, *195*, 109577. https://doi.org/10.1016/j.triboint.2024.109577.
8. Ye, Y.; Qu, S.; Wei, L.; Li, D.; Huang, C.; Wang, J.; Tao, Z.; Gan, F.; Gao, H.; Zhu, B.; et al. Localized Rail Third-Order Bending Mode Causes High-Order Polygonization of High-Speed Train Wheels. *Mech. Syst. Signal Proc.* **2025**, *223*, 111816. https://doi.org/10.1016/j.ymssp.2024.111816.
9. Kang, X.; Lu, S.; Cui, X.; Zhao, X.; Chen, G.; Cao, Z.; Chen, X. Experimental and Numerical Investigation into the Formation Mechanism of Wheel Polygonal Wear of High-Speed Trains with Wheel Flat Excitation. *Wear* **2025**, *571*, 205800. https://doi.org/10.1016/j.wear.2025.205800.
10. Sun, Q.; Chen, C.; Kemp, A.H.; Brooks, P. An On-Board Detection Framework for Polygon Wear of Railway Wheel Based on Vibration Acceleration of Axle-Box. *Mech. Syst. Signal Proc.* **2021**, *153*, 107540. https://doi.org/10.1016/j.ymssp.2020.107540.
11. Chen, S.; Wang, K.; Zhou, Z.; Yang, Y.; Chen, Z.; Zhai, W. Quantitative Detection of Locomotive Wheel Polygonization under Non-Stationary Conditions by Adaptive Chirp Mode Decomposition. *Rail. Eng. Sci.* **2022**, *30*, 129–147. https://doi.org/10.1007/s40534-022-00272-3.
12. Wang, Q.; Xiao, Z.; Zhou, J.; Gong, D.; Zhang, Z.; Wang, Z.; Wang, T.; He, Y. A Dynamic Detection Method for Polygonal Wear of Railway Wheel Based on Parametric Power Spectral Estimation. *Veh. Syst. Dyn.* **2023**, *61*, 2352–2374. https://doi.org/10.1080/00423114.2022.2117058.
13. Xu, W.; Chi, M.; Cai, W.; Tao, G.; Sun, J.; Zhou, Y.; Liang, S. An Anti-Disturbance Method for on-Board Detection of Early Wheel Polygonal Wear by Weighted Angle-Synchronous Moving Average. *Measurement* **2023**, *216*, 112999. https://doi.org/10.1016/j.measurement.2023.112999.
14. Xie, Q.; Tao, G.; Lo, S.M.; Cai, W.; Wen, Z. High-Speed Railway Wheel Polygon Detection Framework Using Improved Frequency Domain Integration. *Veh. Syst. Dyn.* **2024**, *62*, 1424–1445. https://doi.org/10.1080/00423114.2023.2235032.
15. Xu, W.; Cui, L.; Cai, W.; Wu, X.; Tao, G.; Chi, M.; Liang, S. Enhanced Onboard Quantitative Diagnosis of Wheel Polygonal Wear Using Cepstral-Bayesian Calibrated FRF. *Measurement* **2024**, *234*, 114904. https://doi.org/10.1016/j.measurement.2024.114904.
16. Li, D.; Ye, Y.; Li, F.; Wang, Q.; Tao, Z.; Wei, L.; Shi, H.; Qu, S.; Dai, H. A Model-Based Method for Wheel out-of-Roundness Detection Considering Rail Flexibility and Multi-Wheel Interaction. *Mech. Syst. Signal Proc.* **2025**, *233*, 112745. https://doi.org/10.1016/j.ymssp.2025.112745.
17. Wang, Q.; Xiao, Z.; Zhou, J.; Gong, D.; Wang, Z.; Zhang, Z.; Wang, T.; He, Y. A New DFT-Based Dynamic Detection Framework for Polygonal Wear State of Railway Wheel. *Veh. Syst. Dyn.* **2023**, *61*, 2051–2073. https://doi.org/10.1080/00423114.2022.2100797.

18. Ye, Y.; Zhu, B.; Huang, P.; Peng, B. OORNet: A Deep Learning Model for on-Board Condition Monitoring and Fault Diagnosis of out-of-Round Wheels of High-Speed Trains. *Measurement* **2022**, *199*, 111268. https://doi.org/10.1016/j.measurement.2022.111268.
19. Dong, M.; Chen, S.; Xie, B.; Wang, K.; Zhai, W. A Quantitative Detection Method for Wheel Polygonization of Heavy-Haul Locomotives Based on a Hybrid Deep Learning Model. *Measurement* **2024**, *227*, 114206. https://doi.org/10.1016/j.measurement.2024.114206.
20. Magalhães, J.; Jorge, T.; Silva, R.; Guedes, A.; Ribeiro, D.; Meixedo, A.; Mosleh, A.; Vale, C.; Montenegro, P.; Cury, A. A Strategy for Out-of-Roundness Damage Wheels Identification in Railway Vehicles Based on Sparse Autoencoders. *Railw. Eng. Sci.* **2024**, *32*, 421–443. https://doi.org/10.1007/s40534-024-00338-4.
21. Jorge, T.; Magalhaes, J.; Silva, R.; Guedes, A.; Ribeiro, D.; Vale, C.; Meixedo, A.; Mosleh, A.; Montenegro, P.; Cury, A. Early Identification of Out-of-Roundness Damage Wheels in Railway Freight Vehicles Using a Wayside System and a Stacked Sparse Autoencoder. *Veh. Syst. Dyn.* **2025**, *63*, 232–257. https://doi.org/10.1080/00423114.2024.2333771.
22. Sun, W.; Geng, X.; Thompson, D.J.; Wang, T.; Zhou, J.; Zhang, J. On-Board Identification of Wheel Polygonization of Metro Trains Based on Convolutional Neural Network Regression Analysis and Angular-Domain Synchronous Averaging. *Mech. Syst. Signal Process.* **2025**, *230*, 112587. https://doi.org/10.1016/j.ymssp.2025.112587.
23. Li, Z.; Ma, M. Probabilistic Quantitative Inversion of Wheel Out-of-Roundness Using Probabilistic Learning on Manifolds and Dynamic Model. *Measurement* **2025**, *250*, 117166. https://doi.org/10.1016/j.measurement.2025.117166.
24. Xu, W.; Wen, Z.; Tao, G.; Wu, X.; Yang, C.; Xie, Y.; Cai, W.; Liu, J.; Chi, M.; Liang, S. A Physics-Guided Neural Network with Embedded Multi-Wheel FRF for Robust Wheel Polygonal Wear Diagnosis. *Measurement* **2026**, *270*, 120847. https://doi.org/10.1016/j.measurement.2026.120847.
25. Jiang, J.; Tao, G.; Liang, H.; Zhang, K.; Xie, Q.; Lu, C.; Wen, Z.; Xiao, Q. A Structure Information-Assisted Generalization Network for Fault Diagnosis of out-of-Round Wheels of Metro Trains. *Measurement* **2025**, *244*, 116519. https://doi.org/10.1016/j.measurement.2024.116519.
26. Li, T.; Wu, X.; Luo, Z.; Chen, Y.; He, C.; Ding, R.; Zhang, C.; Yang, J. A Bearing Fault Diagnosis Method under Small Sample Conditions Based on the Fractional Order Siamese Deep Residual Shrinkage Network. *Fractal Fract.* **2024**, *8*, 134. https://doi.org/10.3390/fractalfract8030134.
27. Chen, K.; Zhang, R.; Meng, L.; Zheng, X.; Wang, K.; Wang, H. The Fast Bearing Diagnosis Based on Adaptive GSR of Fault Feature Amplification in Scale-Transformed Fractional Oscillator. *ISA Trans.* **2025**, *157*, 124–141. https://doi.org/10.1016/j.isatra.2024.11.044.
28. Gai, Y.; Qiao, Z.; Lu, Y.; Zhu, R.; Zhang, X. Fractional-Order Stochastic Resonance-Based Rescaling-Frequency Scanning Images for Early Multi-Frequency Fault Detection of Machines. *Mech. Syst. Signal Process.* **2026**, *247*, 113944. https://doi.org/10.1016/j.ymssp.2026.113944.
29. Xu, X.; Li, B.; Qiao, Z.; Shi, P.; Shao, H.; Li, R. Caputo-Fabrizio Fractional Order Derivative Stochastic Resonance Enhanced by ADOF and Its Application in Fault Diagnosis of Wind Turbine Drivetrain. *Renew. Energy* **2023**, *219*, 119398. https://doi.org/10.1016/j.renene.2023.119398.
30. He, Y.; Qiao, Z.; Xie, B.; Ning, S.; Li, Z.; Kumar, A.; Lai, Z. Two-Stage Benefits of Internal and External Noise to Enhance Early Fault Detection of Machinery by Exciting Fractional SR. *Chaos Solitons Fractals* **2024**, *182*, 114749. https://doi.org/10.1016/j.chaos.2024.114749.
31. Xie, F.; Niu, K.; Song, Z.; Wang, S.; Chen, H.; Cao, Y. Fractional-Order-Enhanced Dual-View Representation and VibrMamba–VMamba Collaborative Modeling for Gearbox Fault Diagnosis. *Fractal Fract.* **2026**, *10*, 342. https://doi.org/10.3390/fractalfract10050342.
32. Yu, Y.; He, Y.; Karimi, H.R.; Gelman, L.; Cetin, A.E. A Two-Stage Importance-Aware Subgraph Convolutional Network Based on Multi-Source Sensors for Cross-Domain Fault Diagnosis. *Neural Netw.* **2024**, *179*, 106518. https://doi.org/10.1016/j.neunet.2024.106518.
33. Ezard, B.; Li, L.; Hao, H.; Wang, R.; An, S. Robust Structural Damage Detection with Deep Multiple Instance Learning for Sensor Fault Tolerance. *Eng. Struct.* **2025**, *331*, 119957. https://doi.org/10.1016/j.engstruct.2025.119957.
34. Asadi, R.; Yla-Autio, A.; Wiikinkoski, O.H.; Ituarte, I.F. Multimodal Deep Learning-Based on and off-Axis Melt Pool Monitoring for Layer Height and Surface Metrology Predictions in Directed Energy Deposition. *J. Intell. Manuf.* **2026**, *37*, 3995–4022. https://doi.org/10.1007/s10845-025-02714-1.

35. Geng, J.; Li, P.; Tuo, S.; Luo, Z. FiLM-DiffRec: Lightweight Feature-Wise Modulation for Enhanced Timestep Conditioning in Diffusion Recommender Systems. *Expert Syst. Appl.* **2026**, *314*, 131478. https://doi.org/10.1016/j.eswa.2026.131478.
36. Zhang, X.; Song, Y.; Xu, C. FO-FCGFNet: A Fractional-Order Image Processing and Fractal Complexity-Guided Intelligent Estimation Method for Fault Diagnosis in Oil-Immersed Transformer Complex Systems. *Fractal Fract.* **2026**, *10*, 587. https://doi.org/10.3390/fractalfract10080587.

Disclaimer/Publisher's Note: The statements, opinions and data contained in all publications are solely those of the individual author(s) and contributor(s) and not of MDPI and/or the editor(s). MDPI and/or the editor(s) disclaim responsibility for any injury to people or property resulting from any ideas, methods, instructions or products referred to in the content.